



# Perovskite-Derived Pt–Ni/Zn(Ni)TiO<sub>3</sub>/SiO<sub>2</sub> Catalyst for Propane Dehydrogenation to Propene

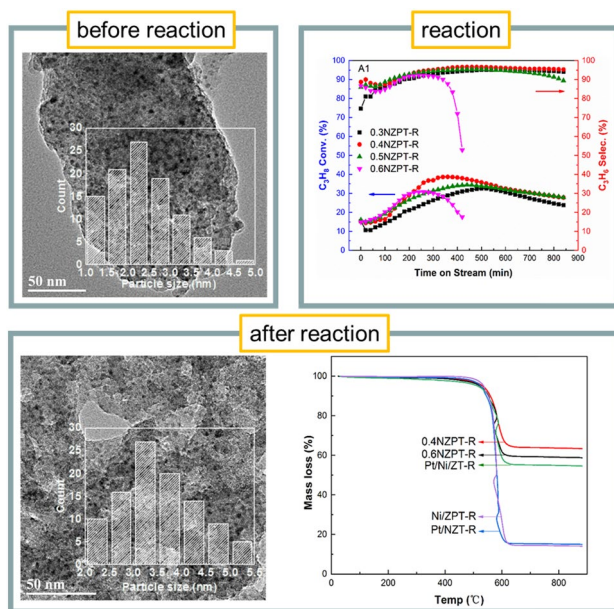
Yatian Liu<sup>1</sup> · Yanyong Li<sup>1</sup> · Meng Ge<sup>1</sup> · Xingye Chen<sup>1</sup> · Mengquan Guo<sup>1</sup> · Lihong Zhang<sup>1</sup>

Received: 14 February 2019 / Accepted: 4 June 2019 / Published online: 11 June 2019  
 © Springer Science+Business Media, LLC, part of Springer Nature 2019

## Abstract

Platinum-based catalysts are promising materials for the propane dehydrogenation (PDH). The Pt sintering and carbon deposition are still the urgent problems to be solved in this system. This paper investigates an investigation of effect of perovskite-type oxide (PTO) lattice confinement on the catalytic performance of Zn(Ni)TiO<sub>3</sub>/SiO<sub>2</sub> supported Pt–Ni bimetallic catalysts for PDH. The supported PTO precursors and derived catalysts were analyzed by XRD, H<sub>2</sub>-TPR, TEM, XPS and TG techniques. The results show that the Pt–Ni alloy nanoparticles (NPs) are formed and highly dispersed on Zn(Ni)TiO<sub>3</sub>/SiO<sub>2</sub>. The optimized Pt loading amount is 0.4 wt%, which enhances the propane conversion to 38.6% and propene selectivity of 96.6%. The superior catalytic performance and anti-sintering and carbon deposition ability of Pt–Ni/Zn(Ni)TiO<sub>3</sub>/SiO<sub>2</sub> catalyst are ascribed to the addition of appropriate Pt amount, which is beneficial to being confined in PTO lattice and building the abundant Pt–Ni alloy sites and moderate Pt–Ni interaction. The unconfined Pt coming from excessive Pt addition and impregnated Pt can result in Pt sintering and carbon formation.

## Graphic Abstract



**Keywords** Perovskite lattice confinement · Propane dehydrogenation · Pt–Ni alloy · Carbon deposition · Pt sintering

✉ Lihong Zhang  
 zlh\_224@163.com

Extended author information available on the last page of the article

## 1 Introduction

Propene is an important raw material in producing polymeric materials such as polypropylene, cumene, acrylic acid and acrylonitrile [1, 2]. With the industrial development, the market demand of propene has been far beyond the production capacity of propene by catalytic cracking process. At present, the direct propane dehydrogenation (PDH) technology is the best way to utilize propane resource and the most competitive production process of propene [3].

Industrially, the catalyst Pt/Al<sub>2</sub>O<sub>3</sub> is widely applied in commercial PDH processes [4]. However, the PDH is not only an endothermic and equilibrium limited reaction, but also requires a low pressure and a high reaction temperature [5]. The high reaction temperature will lead to lower carbon alkane cracking reaction and deep dehydrogenation, which will lower the reaction selectivity, and deep dehydrogenation will cause olefin polymerization and condensation reaction, resulting in catalyst carbon deactivation. At the same time, the high temperature can cause the Pt aggregation and sintering deactivation [6]. In addition, the bond breaking, polymerization and isomerization reactions are also likely to occur at the acidic center of the support Al<sub>2</sub>O<sub>3</sub>, thereby further decreasing the selectivity and increasing carbon deposition [7]. That is to say, the key to the direct PDH technology is to develop Pt-based catalysts with excellent activity, selectivity and stability [8]. Among them, it is crucial to improve the anti-sintering and anti-carbon deposition of Pt-based catalysts [9].

In response to the above problems, the researches about Pt-based catalysts are mainly focused on the modification of additives and supports. Industrially, the support is most widely used in the form of spherical Al<sub>2</sub>O<sub>3</sub>. According to the report [10], the metal oxide support without acid sites can inhibit the formation of carbon deposits and the sintering of supported metals. For example, Mg(Al)O or calcined hydrotalcite-like materials have received extensive attention due to their moderate alkalinity and thermal stability [11]. At present, the additives reported for this system mainly focus on alkali metals (Li, Na, K), alkaline earth metals (Mg, Sr, Ba), transition metals (Fe, Co, Ni, Cu, Zn,) and rare earth metal elements (La, Ce, Y). However, the previous research results were mostly based on impregnated Pt samples. Little attention was paid to the effects of the lattice-confined Pt on the catalytic performances in PDH. Therefore, it is worthwhile to design and prepare a high activity Pt-based catalyst and further understand the structure-performance relationship and interaction among active species, additives and supports.

Perovskite-type oxide (PTO) is a class of complex oxide usually written as ABO<sub>3</sub>. The metal ions A and B can have

a variety of oxidation states (A<sup>+2</sup>B<sup>+4</sup>O<sub>3</sub>, A<sup>+3</sup>B<sup>+3</sup>O<sub>3</sub>, and A<sup>+1</sup>B<sup>+5</sup>O<sub>3</sub>) [12]. Also, the ions at A-site or B-site can be completely or partially replaced by other metal ions with same valence state and similar ionic radius, resulting in a general formula of A<sub>x</sub>A'<sub>1-x</sub>B<sub>y</sub>B'<sub>1-y</sub>O<sub>3</sub> [13] to adjust its redox and surface properties. Moreover, the metal ions at A and B sites in the PTO are well dispersed at atomic level, and the reducible metal ions easily migrate to the surface of the PTO under reducing atmosphere [14, 15].

Considering the dispersion effect of Zn<sup>2+</sup> ions on the stability and interaction of other metal ions [16] and the electron transfer effect of Ti<sup>4+</sup> on the desorption of products and the resistance of carbon deposits [8], ZnTiO<sub>3</sub> PTO was chosen as the framework structure in this paper. In order to stabilize the supported Pt-based catalysts against sintering, Pt<sup>4+</sup> ions were introduced into ZnTiO<sub>3</sub> PTO lattice by partially replacing Ti<sup>4+</sup> ions. Given that the excellent dehydrogenation performance of Ni-based catalysts [17], replacing Zn<sup>2+</sup> ions partially with Ni<sup>2+</sup> ions to obtain Zn(Ni)Ti(Pt)O<sub>3</sub>/SiO<sub>2</sub> is considered in this paper. The physico-chemical properties of the supported PTO precursors and derived catalysts are elucidated upon characterization techniques. The structure-performance relationships are also discussed.

## 2 Experimental

### 2.1 Catalyst Preparation

A series of Zn(Ni)Ti(Pt)O<sub>3</sub>/SiO<sub>2</sub> with different Ni and Pt content were prepared by an incipient impregnation method combined with citric acid and ethylene glycol complexation [18]. Briefly, nickel nitrate, zinc nitrate, chloroplatinic acid and butyl titanate were dissolved in distilled water. Then, the citric acid and ethylene glycol were added in the mixture and stirred until transparent (the total metal ions: citric acid: ethylene glycol molar ratio of 1.00: 1.20: 0.24). And then, the SiO<sub>2</sub> (specific surface area, 347.5 m<sup>2</sup>/g; mean pore diameter, 9.4 nm; total pore volume, 0.91 mL/g) was immersed into the mixed solution for 24 h at room temperature. After that, the solid was dried at 80 °C for 6 h and 120 °C for 12 h and then calcined at 350 °C for 2 h and 700 °C for 5 h, respectively. The obtained Zn(Ni)Ti(Pt)O<sub>3</sub>/SiO<sub>2</sub> precursors are designated as γNZPT (γ stands the mass fraction of Pt in the samples and γ = 0.3, 0.4, 0.5 and 0.6) with Ni/(Ni + Zn) molar ratio of 0.2 (γ = 0, 0.3, 0.4, 0.5 and 0.6, the mass fraction of Pt/(Pt + Ti)). The mass fraction of γNZPT on SiO<sub>2</sub> support is maintained at 20 wt%. For comparison, the SiO<sub>2</sub> supported Pt/NiZnTiO<sub>3</sub>, Pt/Ni/ZnTiO<sub>3</sub>, and Ni/ZnPtTiO<sub>3</sub> were synthesized by impregnating nickel nitrate and/or chloroplatinic acid and labeled as Pt/NZT, Pt/Ni/ZT and Ni/ZPT, respectively, and the Pt content is consistent with 0.4NZPT.

After reduction, the suffix “R” is added at the end of these abbreviated names.

## 2.2 Catalyst Characterization

X-ray diffraction (XRD) (Panalytical X'Pert Pro X-ray diffractometer) was performed at 40 kV and 40 mA with Cu K $\alpha$  radiation ( $\lambda = 0.15406$  nm). Temperature programmed reduction (TPR) was measured in tp 5080 Automatic multi-purpose adsorption instrument. Before the experiment, 50 mg of calcined samples were pretreated in N<sub>2</sub> (40 mL/min) at 500 °C for 1 h to remove surface impurities. The H<sub>2</sub>-TPR data were then obtained by reducing the samples from 30 to 900 °C at 10 °C/min in a stream of 5% H<sub>2</sub>/N<sub>2</sub>, and hydrogen consumption was monitored by a thermal conductivity detector (TCD). X-ray photoelectron spectroscopy (XPS) was conducted on Perkin-Elmer PHI 5000C ESCA with Al K $\alpha$  ( $h\nu = 1253.6$  eV). Transmission electron microscopy (TEM) was performed on JEOL JEM-2100F. Thermogravimetry (TG) was conducted on DTG-50/50H thermal analyzer.

## 2.3 Catalytic Activity Measurement

The catalytic activity tests were conducted in fixed-bed reactor at 600 °C under atmospheric pressure, with 400 mg of the catalyst (40–60 mesh). Before reaction, the catalysts were reduced at 580 °C for 2 h by 5% H<sub>2</sub>/N<sub>2</sub> with a flow rate of 30 mL/min. Then, the gas mixture (the molar ratio of C<sub>3</sub>H<sub>8</sub>: H<sub>2</sub>: N<sub>2</sub> = 8: 7: 35) was introduced into the reactor and reacted on the reduced catalysts. The gaseous products were analyzed by online gas chromatography (GC) using a flame ionization detector (FID).

Propane conversion and product selectivity were calculated as follows [Eqs. (1) and (2)]:

$$\text{Propane conversion (\%)} = \frac{F_{\text{C}_3\text{H}_8, \text{inlet}} - F_{\text{C}_3\text{H}_8, \text{outlet}}}{F_{\text{C}_3\text{H}_8, \text{inlet}}} \times 100\% \quad (1)$$

$$\text{Propane selectivity (\%)} = \frac{F_{\text{C}_3\text{H}_6, \text{outlet}}}{F_{\text{C}_3\text{H}_8, \text{inlet}} - F_{\text{C}_3\text{H}_8, \text{outlet}}} \times 100\% \quad (2)$$

in which  $F_{\text{C}_3\text{H}_8}$  and  $F_{\text{C}_3\text{H}_6}$  represent the molar flow rates of propane and propene, respectively.

## 3 Results and Discussion

### 3.1 Phase Composition and Pt–Ni Interaction of Fresh Catalysts

#### 3.1.1 XRD

The XRD patterns of the calcined precursors of  $\gamma$ NZPT ( $\gamma = 0, 0.3, 0.4, 0.5, 0.6$ ), Pt/NZT, Pt/Ni/ZT, Ni/ZPT and corresponding reduced catalysts are shown in Fig. 1. It can be found that the XRD patterns of all calcined precursors in Fig. 1a exhibits characteristic peaks of PTO materials [PDF file No. 26-1500] at  $2\theta$  of 35.2°, 56.6°, 62.2°, indexed as (110), (108), and (214) planes, respectively. The broad and well-defined diffraction peaks indicate that the obtained PTO NPs are small and poorly crystallized. There is a slight shift of (110) diffraction toward low  $2\theta$  angles from 0NZPT without Pt element to  $\gamma$ NZPT with Pt element. This attributes to the substitution of some smaller hexacoordinate Ti<sup>4+</sup> ions (0.605 Å, Shannon ionic radii [19]) by the bigger hexacoordinate Pt<sup>4+</sup> ions (0.625 Å, Shannon ionic radii [19]) in the PTO lattice. Besides, the PTO (110) peaks become broad with the increasing Pt. This means that the crystallite size of

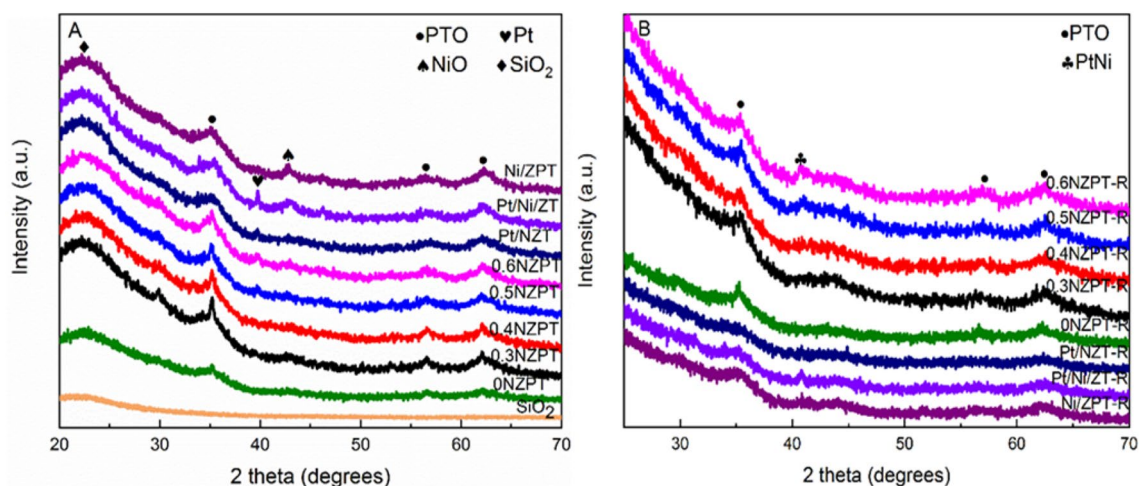


Fig. 1 XRD patterns of the calcined precursors (a) and the reduced catalysts (b)

**Table 1** Crystal size of PTO phase in the calcined precursors<sup>a</sup>

Samples	0.3NZPT	0.4NZPT	0.5NZPT	0.6NZPT
Crystal size (nm)	4.2	3.0	2.9	2.5

<sup>a</sup>Crystal sizes of PTO (110) calculated from Scherrer equation using fwhm of PTO (110) reflection

PTO decreases with the increase of Pt doping. The crystallite size also can be estimated from the value of the full width at half-maximum (fwhm) of (110) diffraction peak by means of the Scherrer equation [20]. The values given in Table 1 show that the crystallite sizes in the (110) direction are exactly correlated with the Pt content.

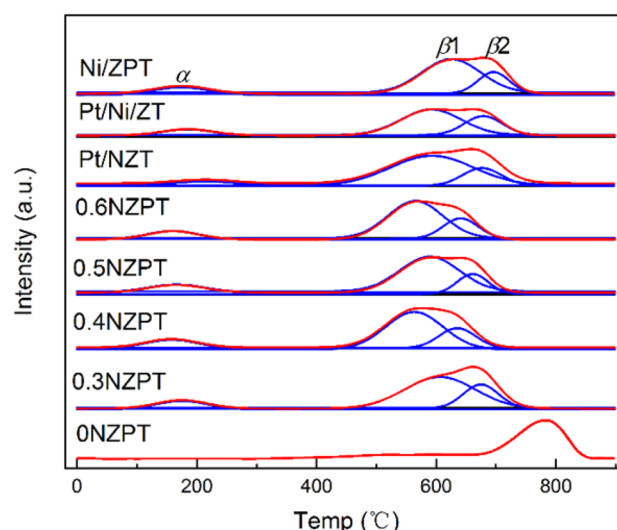
Meanwhile, a weak peak of Pt (110) can be seen at 39.8° [PDF file No. 04-0802] when the Pt content increases to 0.5% and 0.6%. This phenomenon is due to the fact that the Pt substitution can lead to PTO lattice distortion, and the excessive Pt cannot be introduced into the lattice structure. Furthermore, the more Pt content outside of the lattice, the bigger Pt crystallite size forming on the surface of the PTO. Therefore, the Pt peak intensity of 0.6NZPT is slightly stronger than that of 0.5NZPT.

As for the reference sample of Pt/Ni/ZT with the same Ni content of 0.4NZPT, the relatively strong diffraction peaks of Pt and NiO (200) [PDF file No. 02-1216] appear together. This ascribes that the weak Van der Waals force interaction between impregnated Pt<sup>4+</sup> and Ni<sup>2+</sup> ions and support results in aggregation of Pt and NiO nanoparticles (NPs). Similarly, the relatively weak Pt peak and NiO peak can be detected in Pt/NZT and Ni/ZPT respectively. That is to say, it is possible to obtain small metal NPs after reduction for 0.4NZPT. The small Pt and NiO NPs should be attributed to the stabilizing of lattice-confined Ni<sup>2+</sup> and Pt<sup>4+</sup> ions respectively.

According to the XRD patterns in Fig. 1b, it can be found that the PTO phase is well retained in the reduced samples. It plays an important role to stabilize the active metal sites in the PDH reaction. Notably, the original diffraction peaks of Pt and NiO disappear followed by a new peak at 2 $\theta$  of around 40.8° appearing in the reduced 0.5NZPT, 0.6NZPT and Pt/Ni/ZT, which can be owned to the formation of large Pt–Ni alloy [21]. From another point of view, it also hints that there are small-sized and highly-dispersed Pt–Ni alloy on the surface of the reduced 0.3NZPT and 0.4NZPT samples. And the small size and high dispersion of metal active sites are advantageous to PDH reaction [22].

### 3.1.2 TPR

TPR profiles of calcined precursors are drawn in Fig. 2 and qualitative data are listed in Table 2. Notably, only one reduction peak at 781 °C can be observed for 0NZPT without Pt element, which must be assigned to the reduction

**Fig. 2** TPR profiles of the calcined precursors

of Ni<sup>2+</sup> ions [23]. For the Pt-containing samples, a low temperature  $\alpha$  peak appears, which can be assigned to the reduction of Pt<sup>4+</sup> to Pt<sup>0</sup>. Additionally, the reduction peak of Ni<sup>2+</sup> ions shifts to a lower temperature and becomes broader, suggesting that the loading of Pt significantly enhances the reducibility of Ni<sup>2+</sup> ions due to the hydrogen overflow effect [24] and makes the reduction peak of Ni<sup>2+</sup> ions split into two peaks of  $\beta 1$  and  $\beta 2$  corresponding to two kinds of Ni<sup>2+</sup> species. The low temperature  $\beta 1$  peak is the reduction peak of Ni<sup>2+</sup> ions interacting with Pt<sup>4+</sup> ions, while the high temperature  $\beta 2$  peak is the isolated Ni<sup>2+</sup> ions without interaction with Pt<sup>4+</sup> ions [25]. Based on the XRD results above, it can be deduced that the  $\beta 1$  peak can be attributed to the formation of Pt–Ni alloy. It can be seen in Table 2 that the relative proportion of  $\beta 1$  peak of 0.4NZPT is slightly higher than that of other samples, indicating that the Pt–Ni alloy content in reduced 0.4NZPT is the highest one. Furthermore, it can be found

**Table 2** Qualitative TPR data of the calcined precursors

Samples	Peak position/ °C			Relative proportion of $\beta 1/(\beta 1 + \beta 2)^a$ (%)
	$\alpha$	$\beta 1$	$\beta 2$	
0.3NZPT	175	606	675	73
0.4NZPT	158	563	635	78
0.5NZPT	166	589	661	76
0.6NZPT	160	565	641	73
Pt/NZT	214	593	676	74
Pt/Ni/ZT	185	592	679	68
Ni/ZPT	177	625	696	74

<sup>a</sup>The relative proportion calculated by corresponding fitted results of TPR profiles



that the lowest reduction temperature of  $\alpha$  and  $\beta$ 1 peak can be achieved in 0.4NZPT. It indicates that 0.4NZPT has the weakest interaction between  $\text{Pt}^{4+}$  ions and other metal ions [26, 27].

### 3.1.3 XPS

The surface chemical states and composition of the metals in  $\gamma$ NZPT-R, Pt/NZT-R, Pt/Ni/ZT-R and Ni/ZPT-R

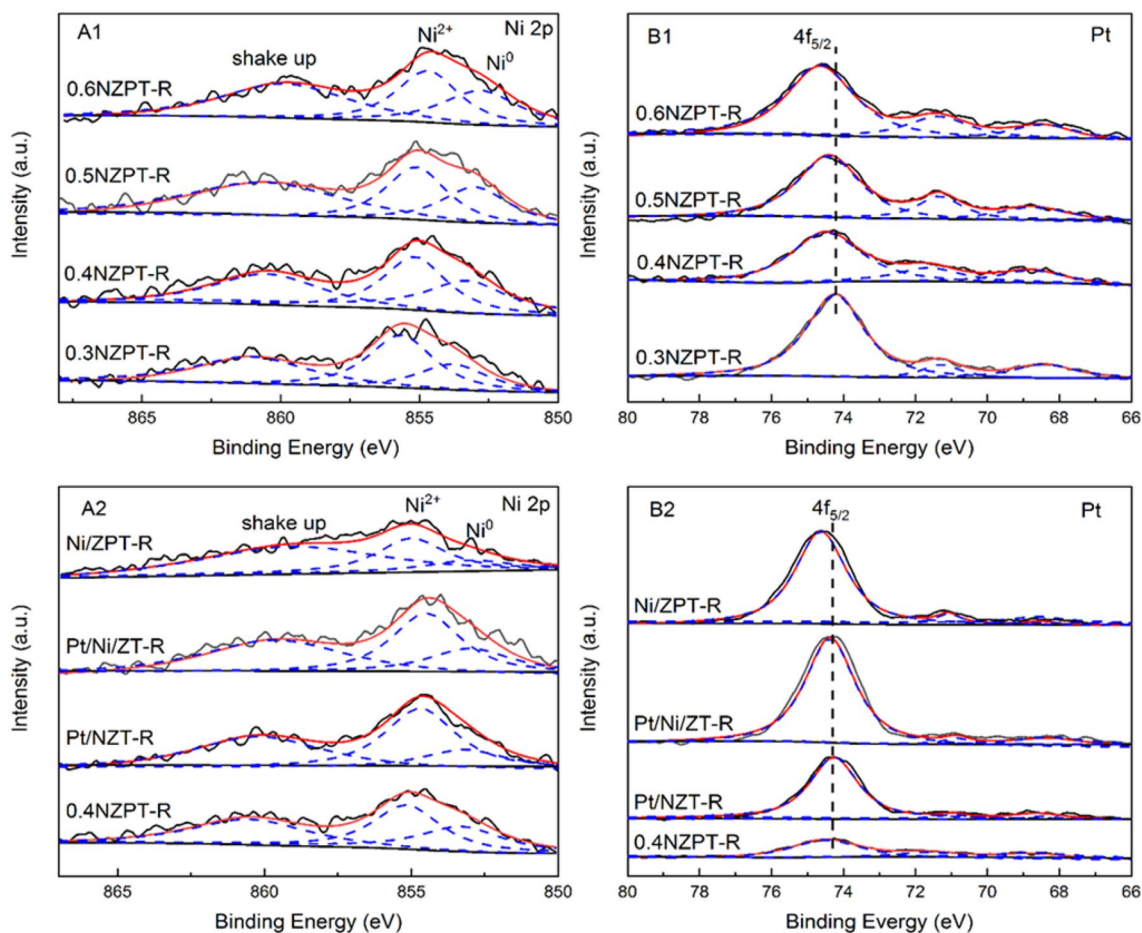


**Fig. 3** XPS of Ni  $2p_{3/2}$  regions and Pt  $4f_{5/2}$  regions in the reduced catalysts

**Table 3** XPS characteristics of Pt  $4f_{5/2}$  and Ni  $2p_{3/2}$  regions for the reduced catalysts

Samples	Binding Energy (eV)			Peak Intensity (%)	Ni/Pt <sup>b</sup>	Ni/Pt <sup>c</sup>
	Pt 4f <sub>5/2</sub>	Ni 2p <sub>3/2</sub>				
	Pt <sup>0</sup>	Ni <sup>2+</sup>	Ni <sup>0</sup>			
				I (Ni <sup>0</sup> ) <sup>a</sup>		
0.3NZPT-R	74.2	855.7	853.7	34.7	8.5	4.7
0.4NZPT-R	74.3	855.2	853.4	40.2	8.1	3.5
0.5NZPT-R	74.4	855.2	853.0	37.3	6.7	2.8
0.6NZPT-R	74.5	854.7	852.8	39.7	5.2	2.3
Pt/NZT-R	74.3	854.7	853.1	25.8	8.5	3.5
Pt/Ni/ZT-R	74.4	854.5	853.0	31.8	8.9	3.5
Ni/ZPT-R	74.6	855.0	853.0	27.1	5.0	3.5

<sup>a</sup>Intensity of the Ni<sup>0</sup> peaks in % of the total Ni  $2p_{3/2}$  area

<sup>b</sup>Detected by XPS analysis

<sup>c</sup>Calculated from the Ni and Pt precursors

were studied by XPS. Figure 3 depicts the Pt 4f<sub>5/2</sub> and Ni 2p<sub>3/2</sub> region spectra of these samples and the corresponding deconvolution results are summarized in Table 3. The analysis of the corresponding Ni 2p<sub>3/2</sub> region shows the presence of two peaks in the range from 850 to 868 eV (Fig. 3a). The peaks appear at binding energy (BE) of ca. 853.0 and 855.0 eV can be attributed to Ni<sup>0</sup> and Ni<sup>2+</sup> ions in the reduced catalysts, respectively literature [28]. As shown in Fig. 3b, there is one peak at ca. 74.4 eV corresponding to Pt<sup>0</sup> in the reduced catalysts [29]. It is well known that the peak position depends on the crystalline structure, chemical composition, near environment and substituent content of metal ions content. In our case, a slight decrease BE in both Ni<sup>0</sup> and Ni<sup>2+</sup> ions can be found in the Ni 2p<sub>3/2</sub> region with the increase of Pt substitution and the order from 0.4NZPT-R and Pt/NZT-R to Pt/Ni/ZT-R and Ni/ZPT-R. Simultaneously, the BE value of Pt<sup>0</sup> present an opposite trend. This is arising from the different strength of surface interaction between Pt and Ni species. According to the results of XRD and TPR, the interaction should be coming from the Pt–Ni alloy. It is the relative low electronegative of Pt [30] and appropriate BE of Pt<sup>0</sup> and Ni<sup>0</sup> result in the moderate Pt–Ni interaction in the 0.4NZPT-R. As can be seen in Table 3, the percentages of Ni<sup>0</sup> for  $\gamma$ NZPT-R are higher than that of others. It also can be deduced that the PTO lattice-confined Ni<sup>2+</sup> ions are easier to interact with the Pt<sup>4+</sup> ions in PTO lattice and reduce into Pt–Ni alloy together. It is obvious that the highest Ni<sup>0</sup> content belong to the 0.4NZPT-R, which implies that the proportion of Pt–Ni alloy is the highest one. This result is consistent with the TPR.

### 3.1.4 TEM

The representative TEM and high resolution TEM (HR-TEM) images of 0.4NZPT-R, 0.6NZPT-R and Pt/Ni/ZT-R are shown in Fig. 4. According to the HR-TEM image of 0.4NZPT-R, the spacing of the lattice fringes of metal NPs is about 0.207 nm, which falls between 0.203 nm of Ni (111) plane and 0.227 nm of Pt (111) plane, therefore it should be assigned to Pt–Ni (111) alloy [21]. Furthermore, the lattice fringe spacing (0.217 nm) of Pt–Ni alloy in the 0.6NZPT-R and Pt/Ni/ZT-R catalysts are larger than that (0.207 nm) observed in the 0.4NZPT-R sample. Additionally, the Ni (111) phase also can be easily found over the reduced Pt/Ni/ZT, which can be determined by the lattice fringe spacing of 0.203 nm. These assignments agree well with the XRD result. And the PSD of 0.4NZPT-R is narrower than that of 0.6NZPT-R and Pt/Ni/ZT-R. Particularly, the most probable particle size of 0.4NZPT-R is only 2.3 nm, which is smaller than that of 0.6NZPT-R (2.8 nm) and Pt/Ni/ZT-R (3.2 nm). This illustrates that it is an effective method to obtain small Pt–Ni alloy by confining Pt<sup>4+</sup> and Ni<sup>2+</sup> ions in the PTO lattice structure together, which is advantageous to the PDH

reaction by restraining the active metal NPs agglomeration and growth.

## 3.2 Characterization of the used Catalysts

### 3.2.1 TEM

As shown in Fig. 5, TEM images are utilized to illuminate the morphology, PSD and phase structure of representative catalysts after PDH reaction. Compared with the images in Fig. 4, the most probable particle size of 0.4NZPT-R, 0.6NZPT-R and Pt/Ni/ZT-R has a slight increase from 2.3 to 3.5 nm, 2.8 to 3.9 nm and 3.2 to 4.7 nm, respectively. Namely, the size and PSD of the used 0.4NZPT-R are still smaller and narrower than those of others during the reaction. The results indicate that the PTO lattice atomic-confined reduction of Pt-based catalysts significantly improves sintering resistance by suppressing effect of the PTO lattice for the agglomeration of the metal NPs involving Pt–Ni alloy, Pt and Ni species, which can result in the outstanding stability of 0.4NZPT-R catalyst. From HR-TEM images, some carbon deposits also can be observed on these used samples. And even the Ni (111) planes also can be found on the used 0.6NZPT-R and Pt/Ni/ZT-R. This can be attributed to the Ni sintering after reaction. It further can be determined that the catalyst 0.4NZPT-R exhibits excellent resistance to sintering.

### 3.2.2 TG

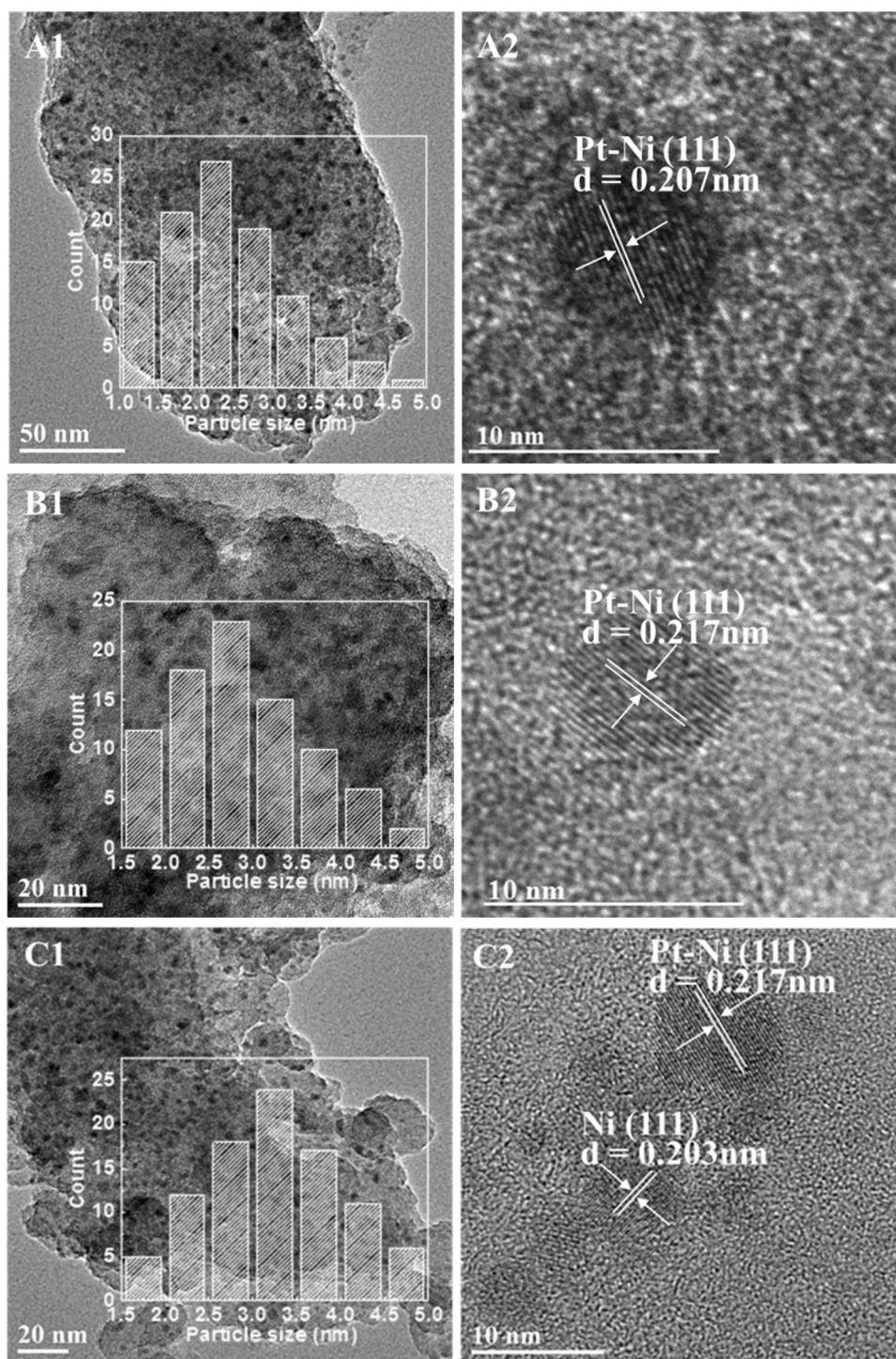
The amount of carbon deposition can be determined by TG. Figure 6 shows the mass loss profiles of representative catalysts after PDH reaction. It is obvious that the order of carbon deposition is as followed: 0.4NZPT-R < 0.6NZPT-R < Pt/Ni/ZT-R < Pt/NZT-R < Ni/ZPT-R. Combining with the XRD, TPR and TEM results, the high content and moderate interaction of Pt–Ni alloy and small particle size are good for resistance to carbon deposition.

## 3.3 Catalytic Activity

Figure 7 shows the change in propane conversion and the selectivity of propene and methane over time. As can be seen from Fig. 7, the reaction process over all catalysts could be divided into three stages: induction, stable and deactivated period [27].

From Table 3, it can be observed that the Ni/Pt ratio in the catalysts is considerably higher than the value calculated from the Ni and Pt precursors. This indicates the enrichment of Ni on the surface of the catalyst. Sun et al. [31] also proposed a similar viewpoint. These all indicate that the induction period is due to the in situ creation of Ni<sup>0</sup> species generated from the catalysts under reductive atmosphere [27,

**Fig. 4** TEM images, the statistics of particle size distribution in inset and HR-TEM: **a** 0.4NZPT-R, **b** 0.6NZPT-R and **c** Pt/Ni/ZT-R



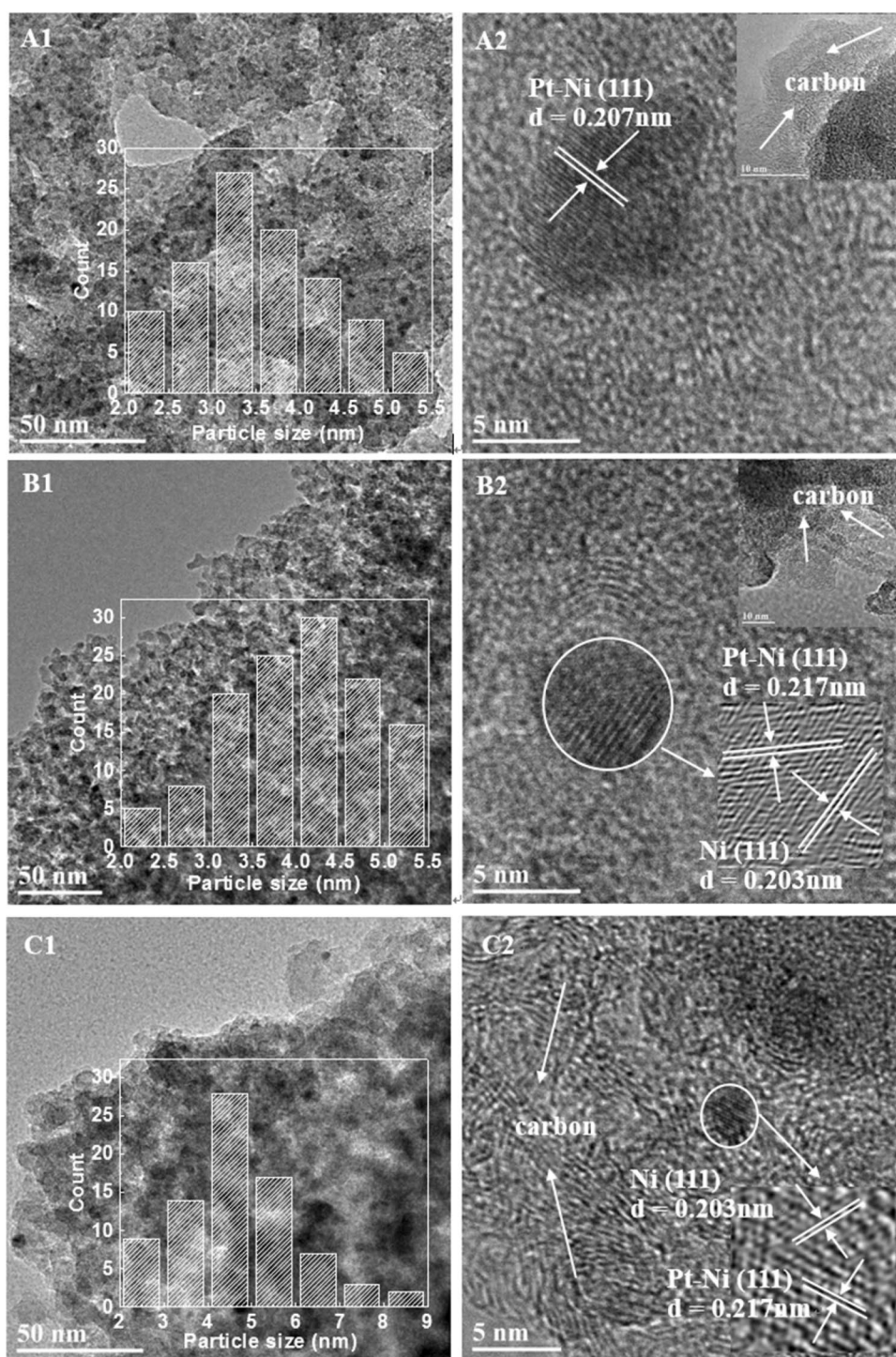
32, 33], and this specific  $\text{Ni}^0$  species are confirmed to interact with Pt to form some active sites for dehydrogenation.

In Fig. 7a1 and a2, the 0.4NZPT-R shows the highest propane conversion, propene selectivity and the lowest methane selectivity. According to the structural analysis above, it should be related to the high content, small size and moderate interaction of Pt–Ni alloy in 0.4NZPT-R. These features also can be used to explain the longest stabilizing period

of the 0.4NZPT-R. The 0.3NZPT-R possesses the lowest activity among the  $\gamma$ NZPT-R samples. It is related to the lowest Pt content. However, compared with 0.4NZPT-R, the higher Pt content in the 0.5NZPT-R also cannot improve the dehydrogenation activity. It should be related to the low content and big particle size of Pt–Ni alloy in 0.5NZPT-R. The same reason can be used to explain the low propane conversion of 0.6NZPT-R. It is worth noting that there is a



**Fig. 5** TEM images of the reduced catalysts after reaction: **a** 0.4NZPT-R, **b** 0.6NZPT-R and **c** Pt/Ni/ZT-R



slight decline of the propene selectivity along with a slight rise of methane over 0.5NZPT-R after 600 min. As for the 0.6NZPT-R, there is a sudden production of methane and decrease of propene after 250 min. According to the XRD and TEM results of 0.6NZPT-R, it can be deduced that the sintering of metal NPs becomes more and more severe during the reaction. These phenomena indicate that the particle size of metal NPs over the 0.5NZPT-R and 0.6NZPT-R has

become big enough to make propane prone to cracking into methane after 600 and 250 min respectively. The sudden production of methane over the 0.6NZPT-R must be related to the fast sintering of metal NPs.

As shown in Fig. 7b1 and b2, the catalytic behavior for PDH over the 0.4NZPT-R is superior to that over the Pt/Ni/ZT-R, Pt/Ni/ZT-R and Ni/ZPT-R. The reasons for the PDH behavior of the 0.6NZPT-R can be used to explain that of the



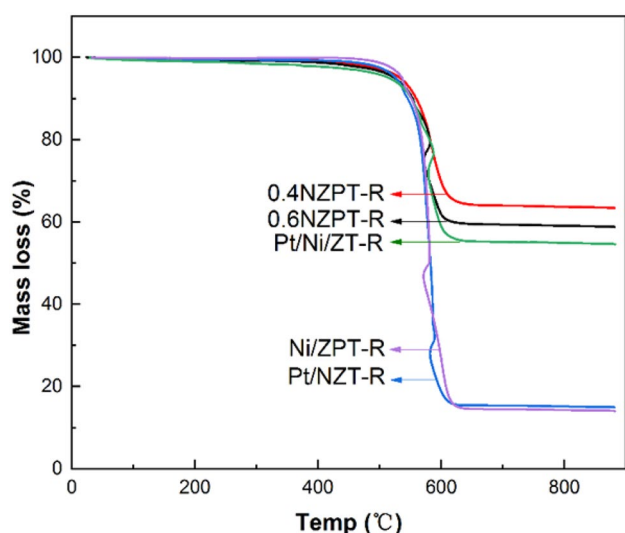


Fig. 6 TG curves of the reduced catalysts after reaction

Pt/NZT-R and Ni/ZPT-R. The selectivity of 0.4NZPT-R and Pt/Ni/ZT-R for methane is almost the same, the difference is that neither Pt nor Ni are introduced into the PTO lattice in Pt/Ni/ZT-R, resulting in the formation of large metal NPs, and the amount of alloy in Pt/Ni/ZT-R is relatively less than 0.4NZPT-R. Therefore, the activity of Pt/Ni/ZT-R is lower than that of 0.4NZPT-R. This indicates that the metal active species acquired from PTO lattice atomic-confined reduction can easily form alloy and effectively inhibit the agglomeration. In other word, the PTO lattice structure can effectively resist carbon deposition, metal sintering and propane cracking during PDH.

Finally, a comparison between works with studied here and previously reported in literatures [4, 8, 33–35] for PDH has been listed in Table 4. It is remarkable that our results demonstrate that the PTO lattice confinement stabilizing Pt–Ni based catalysts can reduce metal particle size and achieve relatively high conversion, selectivity and stability with lower Pt content, which have application prospects in the field of PDH.

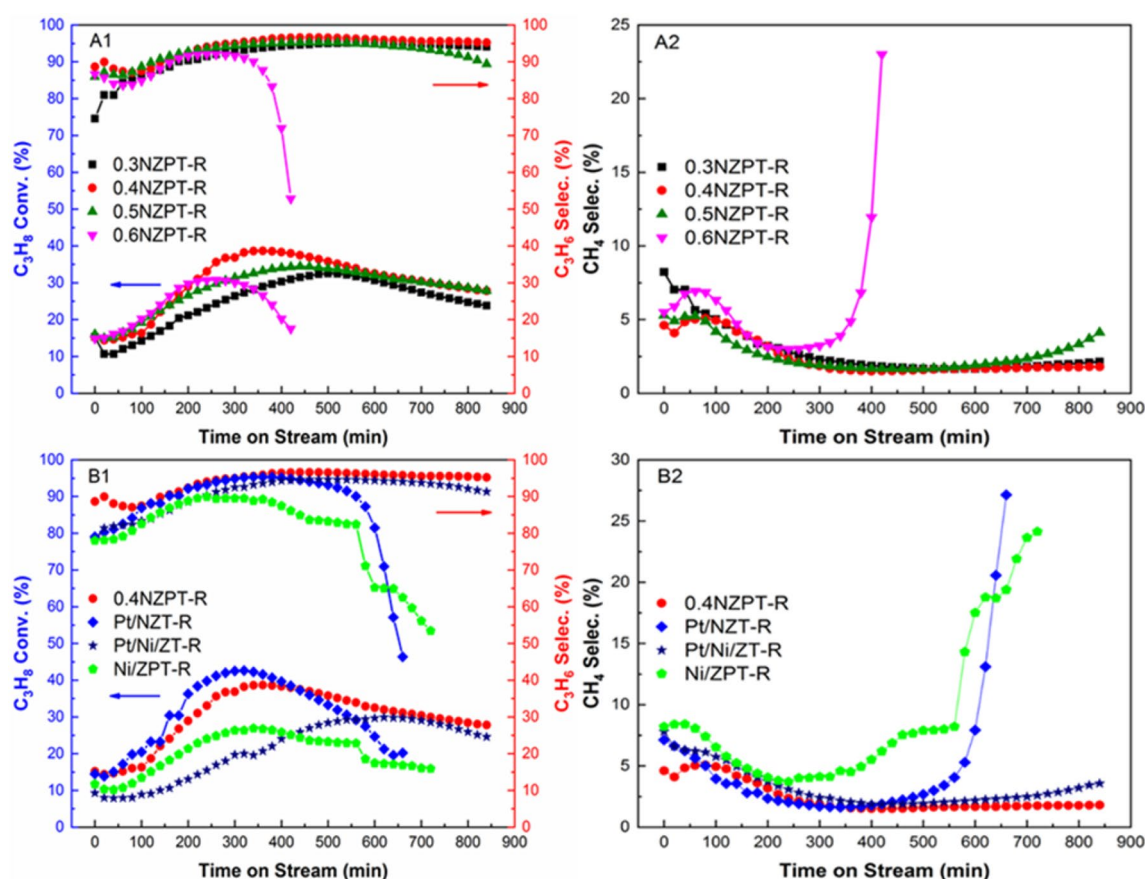


Fig. 7 Propane conversion, propene and methane selectivity as functions of time for **a**  $\gamma$ NZPT-R ( $\gamma=0.3, 0.4, 0.5, 0.6$ ) and **b** 0.4NZPT-R, Pt/NZT-R, Pt/Ni/ZT-R and Ni/ZPT-R

**Table 4** Comparison of catalytic performance of various catalysts in propane dehydrogenation

Catalysts	Pt contents (wt%)	WHSV (h <sup>-1</sup> )	Reaction temperature (°C)	Propane conversion (%)	Propene selectivity (%)	References
0.4NZPT	0.4	3	600	38.6	96.6	Present work
PtNi/SBA-15	0.75	3.43	600	60	42	[34]
Pt/TiO <sub>2</sub> –Al <sub>2</sub> O <sub>3</sub>	1	10	600	47.3	89.5	[8]
Pt–Cu/Al <sub>2</sub> O <sub>3</sub>	0.5	3	600	44	90.8	[4]
PtNa/Zn–ZSM-5	0.5	3	590	40.6	97	[35]
PtIn/Mg(Al)O	0.6	3.3	620	61	96	[33]

## 4 Conclusions

A series of supported Pt-based PTO catalysts Zn(Ni)Ti(Pt)O<sub>3</sub>/SiO<sub>2</sub> can be obtained by an incipient impregnation method combined with citric acid and ethylene glycol complexation. The PTO lattice confinement has a significant influence on the structure and catalytic performance of catalysts in the propane dehydrogenation (PDH) to propene reaction. The PTO lattice confined Pt and Ni are prone to form small Pt–Ni alloy. The abundant Pt–Ni alloy sites and moderate Pt–Ni interaction in Pt–Ni/Zn(Ni)TiO<sub>3</sub>/SiO<sub>2</sub> with Pt content of 0.4 wt% are indicative of higher capability to resist carbon deposition and metal sintering and thus are helpful to the improvement of catalytic activity and selectivity.

**Acknowledgements** This study was supported by the National Natural Science Foundation of China (No. 21776214) and State Key Laboratory of Chemical Resource Engineering.

## Compliance with Ethical Standards

**Conflict of interest** The authors declare no conflict of interest.

## References

- Watanabe R, Sekine Y, Kojima J, Matsukata M, Kikuchi E (2011) Dehydrogenation of ethylbenzene over highly active and stable perovskite oxide catalyst-effect of lattice oxygen on/in perovskite oxide and role of A/B site in perovskite oxide. *Appl Catal A* 398(1):66–72
- Jin SH, Guan WX, Tsang CW, Yan DYS, Chan CY, Liang CH (2017) Enhanced hydroconversion of lignin-derived oxygen-containing compounds over bulk nickel catalysts through Nb<sub>2</sub>O<sub>5</sub> modification. *Catal Lett* 147(8):2215–2224
- Mcgregor J, Huang ZY, Parrott EPI, Zeitler JA, Nguyen KL, Jeremy MR, Rawson JM, Carley A, Hansen TW, Tessonier JP, Su DS, Teschner D, Vass EM, Knop-Gericke A, Schlögl R, Gladden LF (2010) Active coke: carbonaceous materials as catalysts for alkane dehydrogenation. *J Catal* 269:329–339
- Han ZP, Li SR, Jiang F, Tuo W, Ma XB, Gong JL (2014) Propane dehydrogenation over Pt–Cu bimetallic catalysts: the nature of coke deposition and the role of copper. *Nanoscale* 6:10000–10008
- Lee H, Kim WI, Jung KD, Koh HL (2017) Effect of Cu promoter and alumina phases on Pt/Al<sub>2</sub>O<sub>3</sub> for propane dehydrogenation. *Korean J Chem Eng* 34(5):1337–1345
- Ricca A, Palma V, Iaquaniello G, Palo E, Salladini A (2017) Highly selective propylene production in a membrane assisted catalytic propane dehydrogenation. *Chem Eng J* 330:1119–1127
- Li Q, Sui ZJ, Zhou XG, Zhu Y, Zhou JH, Chen D (2011) Coke formation on Pt–Sn/Al<sub>2</sub>O<sub>3</sub> catalyst in Propane dehydrogenation: coke characterization and kinetic study. *Top Catal* 54(13–15):888–896
- Jiang F, Zeng L, Li SR, Liu G, Wang SP, Gong JL (2015) Propane dehydrogenation over Pt/TiO<sub>2</sub>–Al<sub>2</sub>O<sub>3</sub> Catalysts. *ACS Catal* 5(1):438–447
- Si J, Liu GL, Liu JG, Zhao L, Li SS, Guan Y, Liu Y (2016) Ni nanoparticles highly dispersed on ZrO<sub>2</sub> and modified with La<sub>2</sub>O<sub>3</sub> for CO methanation. *RSC Adv* 15(6):12699–12707
- Dongil AB, Bachiller-Baeza B, Rodriguez-Ramos I, Fierrob JLG, Escalona N (2016) The effect of Cu loading on Ni/carbon nanotubes catalysts for hydrodeoxygenation of guaiacol. *RSC Adv* 6:26658–26667
- Xia K, Lang WZ, Li PP, Long LL, Yan X, Guo YJ (2016) The influences of Mg/Al molar ratio on the properties of PtIn/Mg(Al)O–x catalysts for propane dehydrogenation reaction. *Chem Eng J* 284:1067–1079
- Polo-Garzon F, Yang SZ, Fung V, Foo GS, Bickel EE, Chisholm MF, Jiang DE, Wu ZL (2017) Controlling reaction selectivity through the surface termination of perovskite catalysts. *Angew Chem Int Edit* 56(33):9820–9824
- Sumathi R, Johnson K, Viswanathan B, Varadarajan TK (1998) Selective oxidation and dehydrogenation of benzyl alcohol on ABB'O<sub>3</sub> (A = Ba, B = Pb, Ce, Ti and B' = Bi, Cu, Sb) -type perovskite oxides-temperature programmed reduction studies. *Appl Catal A* 172(1):15–22
- Deng J, Cai M, Sun W, Liao X, Chu W, Zhao XS (2013) Oxidative methane reforming with an intelligent catalyst: sintering-tolerant supported nickel nanoparticles. *ChemSusChem* 6(11):2061–2065
- Fang YZ, Liu Y, Zhang LH (2011) LaFeO<sub>3</sub>-supported nano Co–Cu catalysts for higher alcohol synthesis from syngas. *Appl Catal A* 397:183–191
- Yu CL, Xu HY, Ge QJ, Li WZ (2007) Properties of the metallic phase of zinc-doped platinum catalysts for propane dehydrogenation. *J Mol Catal A* 266(1–2):80–87
- Zhu QQ, Wang GW, Liu JW, Su LS, Li CY (2017) Effect of Sn on isobutane dehydrogenation performance of Ni/SiO<sub>2</sub> catalyst: adsorption modes and adsorption energies of isobutane and isobutene. *ACS Appl Mater Interfaces* 9(36):30711–30721
- Yang X, Liu GL, Li YX, Zhang L, Wang XT, Liu Y (2019) Novel Pt–Ni bimetallic catalysts Pt(Ni)–LaFeO<sub>3</sub>/SiO<sub>2</sub> via lattice atomic-confined reduction for highly efficient isobutane dehydrogenation. *Trans Tianjin Univ* 25(3):245–257

19. Shannon RD (1976) Revised effective ionic radii and systematic studies of interatomic distances in halides and chalcogenides. *Acta Crystallogr A* 32(5):751–767
20. Liu GL, Geng YX, Pan DM, Zhang Y, Niu T, Liu Y (2014) Bi-metal Cu–Co from  $\text{LaCo}_{1-x}\text{Cu}_x\text{O}_3$  perovskite supported on zirconia for the synthesis of higher alcohols. *Fuel Process Technol* 128:289–296
21. Dai H, Qiu YP, Dai HB, Wang P (2018) Ni–Pt/CeO<sub>2</sub> loaded on granular activated carbon: an efficient monolithic catalyst for controlled hydrogen generation from hydrous hydrazine. *ACS Sustain Chem Eng* 26:1–23
22. Zhu J, Yang ML, Yu YD, Zhu YA, Sui ZJ, Zhou XG, Anders H, Chen D (2015) Size-dependent reaction mechanism and kinetics for propane dehydrogenation over Pt catalysts. *ACS Catal* 5(11):6310–6319
23. Han T, Zhao L, Liu GL, Ning HY, Yue YZ, Liu Y (2017) Rh–Fe alloy derived from  $\text{YRh}_{0.5}\text{Fe}_{0.5}\text{O}_3/\text{ZrO}_2$  for higher alcohols synthesis from syngas. *Catal Today* 298:69–76
24. Arenas-Alatorre J, Gomez-Cortes A, Avalos-Borja M, Diaz G (2005) Surface properties of Ni–Pt/SiO<sub>2</sub> catalysts for N<sub>2</sub>O decomposition and reduction by H<sub>2</sub>. *J Phys Chem B* 109(6):2371–2376
25. Jentys A, Mchugh BJ, Haller GL, Lercher JA (1992) Temperature-programmed reduction of silica-supported Pt/Ni catalysts studied by XANES. *J Phys Chem* 96(3):1324–1328
26. Doh H, Kim HY, Kim GS, Cha J, Park HS, Ham HC, Yoon SP, Han J, Nam SW, Song KH, Yoon CW (2017) Influence of cation substitutions based on ABO<sub>3</sub> perovskite materials,  $\text{Sr}_{1-x}\text{Y}_x\text{Ti}_{1-y}\text{Ru}_y\text{O}_{3-\delta}$ , on ammonia dehydrogenation. *ACS Sustain Chem Eng* 5:9370–9379
27. Shen LL, Xia K, Lang WZ, Chu LF, Yan X, Guo YJ (2017) The effects of calcination temperature of support on PtIn/Mg(Al) O catalysts for propane dehydrogenation reaction. *Chem Eng J* 324:336–346
28. Nassr AAA, Sinev I, Pohl MM, Grunert W, Bron M (2014) Rapid microwave-assisted polyol reduction for the preparation of highly active PtNi/CNT electrocatalysts for methanol oxidation. *ACS Catal* 4(8):2449–2462
29. Qiao L, Bi XF (2009) Nanostructure and performance of Pt–LaNiO<sub>3</sub> composite film for ferroelectric film devices. *Acta Mater* 57(14):4109–4114
30. Pastor-Perez L, Sepulveda-Escribano A (2017) Low temperature glycerol steam reforming on bimetallic PtSn/C catalysts: on the effect of the Sn content. *Fuel* 194:222–228
31. Sun YN, Wu YM, Tao L, Shan HH, Wang GW, Li CY (2015) Effect of pre-reduction on the performance of Fe<sub>2</sub>O<sub>3</sub>/Al<sub>2</sub>O<sub>3</sub> catalysts in dehydrogenation of propane. *J Mol Catal A* 397:120–126
32. Chen M, Wu JL, Liu YM, Cao Y, Guo L, He HY, Fan KN (2011) Study in support effect of In<sub>2</sub>O<sub>3</sub>/MO<sub>x</sub> (M = Al, Si, Zr) catalysts for dehydrogenation of propane in the presence of CO<sub>2</sub>. *Appl Catal A* 407(1):20–28
33. Xia K, Lang WZ, Li PP, Yan X, Guo YJ (2015) Analysis of the catalytic activity induction and deactivation of PtIn/Mg(Al) O catalysts for propane dehydrogenation reaction. *RSC Adv* 5(79):64689–64695
34. Cai W, Mu R, Zha S, Sun G, Chen S, Zhao Z, Li H, Tian H, Tang Y, Tao F, Zeng L, Gong J (2018) Subsurface catalysis-mediated selectivity of dehydrogenation reaction. *Sci Adv* 4(8):5418–5426
35. Zhang Y, Zhou Y, Huang L, Zhou S, Sheng X, Wang Q, Zhang C (2015) Structure and catalytic properties of the Zn-modified ZSM-5 supported platinum catalyst for propane dehydrogenation. *Chem Eng J* 270:352–361

**Publisher's Note** Springer Nature remains neutral with regard to jurisdictional claims in published maps and institutional affiliations.

## Affiliations

Yatian Liu<sup>1</sup>  · Yanyong Li<sup>1</sup>  · Meng Ge<sup>1</sup>  · Xingye Chen<sup>1</sup>  · Mengquan Guo<sup>1</sup>  · Lihong Zhang<sup>1</sup> 

<sup>1</sup> Department of Catalysis Science and Technology and Tianjin Key Laboratory of Applied Catalysis Science & Technology, School of Chemical Engineering and Technology, Tianjin University, Tianjin 300350, People's Republic of China